Effect of wave-topography interactions on the formation of sand ridges on the shelf

N. C. Vis-Star,[1] H. E. de Swart,[1] and D. Calvete[2]

[1] The role of wave-topography interactions in the formation of sand ridges on microtidal inner shelves is investigated with an idealized morphodynamic model. The latter uses the two-dimensional shallow water equations to describe a storm-driven flow on an inner shelf with an erodible bottom and a transverse slope. Both bed load and suspended load sediment transport are included. New are the incorporation of a wave module based on physical principles and a critical shear-stress for erosion. A linear stability analysis is used to study the initial growth of bed forms, by analyzing the initial growth of small perturbations evolving on an alongshore uniform basic state, which describes a storm-driven flow on a microtidal inner shelf. Model simulations show that wave-topography interactions cause the ridges to become more trapped to the coast. Both growth and migration of the ridges are controlled by suspended load transport. The physical mechanism responsible for ridge growth is related to transport by the storm-driven current of sediment that is entrained due to wave orbital motions induced by bed forms. This new mechanism even acts in absence of a transverse bottom slope. The orientation, spacing and shape of the modeled ridges agree well with field observations from different shelves.

1. Introduction

[2] A rich variety of sand ridges is observed in coastal and shelf seas. In *Dyer and Huntley* [1999] a classification scheme is presented based on the long-term evolution of the ridges in relation with the present-day hydrodynamic setting. The bed forms that will be considered in this paper are type 2B(ii) in this scheme: the shoreface-connected ridges (hereafter abbreviated as sfcr), which are characterized by crests oriented obliquely with respect to the shoreline. They evolve on inner shelves (depths between 5 and 30 m) where storms occur frequently. Early observations were reported on the most prominently present sfcr along the Atlantic shelf of North America by *Duane et al.* [1972], *Swift et al.* [1972] and *Swift and Field* [1981]. In *Swift et al.* [1978] ridges that occur on European shelves were described. Sfcr were also observed on the Brazilian shelf [*Figueiredo et al.*, 1982], the Argentinean shelf [*Parker et al.*, 1982], the Canadian shelf [*Hoogendoorn and Dalrymple*, 1986; *Amos et al.*, 1996], the Belgian and central Dutch coast [*van de Meene and van Rijn*, 2000], the German shelf [*Antia*, 1996], the Danish shelf [*Anthony and Leth*, 2002] and the West Florida shelf [*Twichell et al.*, 2003; *Edwards et al.*, 2003; *Harrison et al.*, 2003].

[3] A noticeable characteristic of sfcr is their rhythmic structure with a typical alongshore spacing between successive crests of 2–6 km. Lengths of individual crests are between 10 and 25 km and heights range from 1 to 6 m. Both observations [*Swift et al.*, 1978; *Antia*, 1996; *van de Meene and van Rijn*, 2000] and model studies [*Trowbridge*, 1995; *Calvete et al.*, 2001a] indicate that the growth of the ridges takes place during storms. Stormy weather is characterized by high waves (wave heights of 2–4 m) and a mean storm-driven flow of up to 0.5 m s^{-1}. The orientation of the ridges is related to the dominant storm-driven flow. The seaward ends of the crests are shifted up-current with respect to their attachments to the shoreface, thereby making an angle of 10–50° with respect to the coastline. Exceptions to this are the ridges found on the central part of the Danish west coast which have angles of about 60° and the ridges on the west-central Florida shelf which are oriented at angles of 58–75°. All the ridges show a migration in the direction of the storm-driven current with a magnitude of 1–10 m yr^{-1} and they evolve on a timescale of decades to centuries.

[4] Proposed hypotheses on the origin of sfcr can be divided into two broad classes. The first is that the ridges are relict features from before the Holocene transgression [*McClennen and Mcmaster*, 1971; *Swift et al.*, 1972]. The second is that they emerge due to inherent dynamic interactions between the water motion and the sandy bed (called morphodynamic self-organization). Although some features

[1]Institute for Marine and Atmospheric Research Utrecht, Utrecht University, Utrecht, Netherlands.
[2]Departament de Física Aplicada, Universitat Politécnica de Catalunya, Barcelona, Spain.

appear to be largely relict, observations by *Swift et al.* [1978] and *Twichell et al.* [2003] show that sediment transport in ridge areas is significant, especially under stormy conditions. So, even when the ridges have a relict origin, they are often subject to sediment reworking by modern shelf processes. *McBride and Maslow* [1991] argue that ebb-tidal deltas provided the initial sand source for the development of many sfcr and shelf processes act as modifying agents in the evolution during and after ebb-tidal delta deposition.

[5] A process-based model for sfcr, using the second hypothesis of morphodynamic self-organization, was proposed by *Trowbridge* [1995]. His model consists of the depth-averaged shallow water equations, ignoring Coriolis and bottom friction terms. The sediment transport due to bed load is linearly related to the mean flow. The model describes the initial formation of sfcr due to the joint action of waves (stirring sand from the bottom) and a longshore storm-driven flow (causing net sand transport). Trowbridge demonstrated the growth and down-current migration of up-current oriented ridges having similar shape as the observed ridges in the field. The latter is the consequence of a positive coupling between small topographic perturbations superimposed on the mean alongshore uniform equilibrium state and the induced small hydrodynamic perturbations such that sand transport is convergent over the ridges.

[6] The model of *Trowbridge* [1995] was extended by *Falqués et al.* [1998] to include Coriolis terms, bottom shear-stresses and sediment transport due to bottom slopes. The latter was shown to be crucial to obtain a preferred mode of which the spacing agrees with field observations. *Restrepo* [2001] included the effect of a wave-induced Stokes drift in the model and found that it tempered the growth mechanism. However, the ratio of timescales related to growth and migration of the bed forms is not in accordance with field data and the instability mechanism is very sensitive to the cross-shore profile of the storm-driven current.

[7] *Calvete et al.* [2001a] argued that these artefacts were due to the neglect of suspended load sediment transport and spatial variations in stirring of sediment by the waves. The results of their model, which accounts for the processes mentioned above, compare favorably well with field data (both ridge growth and migration). Moreover, the results are hardly sensitive to the profile of the storm-driven flow. A drawback of the model is that it uses a strongly simplified description of waves in calculating the stirring of sediment. The parameterization (derived from a simple wave shoaling model) is such that the amplitude of the near-bed wave orbital motion decreases with increasing water depths (thus also the stirring of sediment by the waves). In fact, in the latter model wave properties only depend on the undisturbed reference depth and refraction, shoaling and dissipation due to the presence of bed forms are ignored.

[8] In a recent study by *Calvete et al.* [2005] a sophisticated wave transformation model was used to study the initial formation of sandbars in the surf zone. They showed that explicit modeling of wave-topography interactions is crucial for obtaining good agreement between model results and field observations. Therefore, in the present paper a morphodynamic model for the inner shelf will be discussed which includes a process-based wave transformation model. This enables the study of interactions between waves and the bottom topography and the effect on the initial growth of sfcr. Important differences with *Calvete et al.* [2005] are a different geometric setting (inner shelf rather than surf zone) and the consideration of obliquely incident waves. The objective is to investigate the effect of the improved wave formulation and in addition the influence of growing bed forms on the wave properties (the latter was not possible before).

[9] The paper is organized as follows. In section 2 a new model will be presented, which extends that of *Calvete et al.* [2001a] with regard to the description of waves and the formulation of sand transport. This is followed in section 3 by an outline of the method of analysis. Results will be presented in section 4 and are followed by a discussion (section 5) on the physical interpretation, agreement with field data and model simplifications. We end with concluding remarks (section 6).

2. Model Formulation

[10] The starting point is a reference shelf geometry. Forcing of the water motion on this shelf is due to wind generating both waves and an alongshore current. Waves affect the current through the bed shear-stress. Forcing of currents due to the divergence of wave-induced radiation stresses, the effect of currents on waves through the Doppler shift and wave diffraction are neglected here. This can be justified by assuming that waves hardly break on the inner shelf and that the typical phase speed of the waves is much larger than the current velocity. It is further assumed that the sediment is transported only during stormy weather, which occurs for a specific time fraction (about 5%). In contrast, during fair weather bottom stresses are not sufficiently strong to erode the sediment particles from the bottom. During storms wave orbital velocity amplitudes are large compared with the mean storm-induced longshore current. The strong near-bed wave orbital motion stirs the sediment from the bottom, which is subsequently transported by the mean flow. The long-term bottom evolution is determined by the wave-averaged sediment transport. Divergence of the sediment transport leads to bottom change and this in turn will affect the hydrodynamics. Positive internal feedbacks between the flow field and the erodible bed of the inner shelf will cause growth of bed forms. Below, details about the different parts of the model are given (equations are representative for storms).

2.1. Shelf Geometry

[11] The reference geometry consists of an inner shelf with a sloping bed and depth increasing in seaward direction. It is bounded on the landward side ($x = 0$) by the transition from inner shelf to shoreface (depth H_0) and on the seaward side ($x = L_s$) by an outer shelf with constant depth H_s. The bottom profile is longshore uniform. The transition from the shoreface to the inner shelf is assumed to be straight and without interruptions. An orthogonal coordinate system is used such that the x-axis points in the cross-shore (seaward) direction and the y-axis in the alongshore direction (pointing into the paper). The z-axis is directed
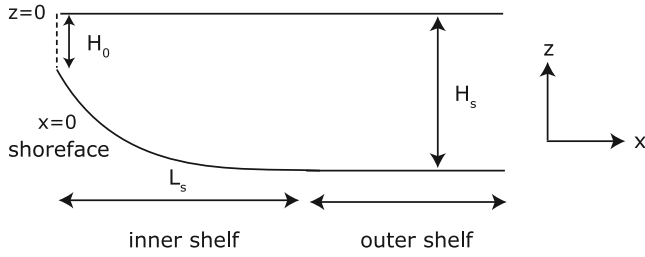
Figure 1. Side view of a typical longshore- and time-averaged bottom topography of the continental shelf, representing the inner and outer shelf, in the shore-normal direction. For explanation of the symbols, see the text.

vertically upward and $z = 0$ represents the still water level. A sketch of the geometry is presented in Figure 1.

2.2. Hydrodynamics

2.2.1. Waves

[12] The wave transformation model is based on linear wave theory. This holds if waves have a small steepness and amplitudes which are much smaller than the water depth. For waves (wind and swell) and water depths we are considering (inner shelf region) this will generally be the case.

[13] Wind-generated waves usually show randomly varying wave heights, periods and directions. *Longuet-Higgins* [1980] discussed the statistical properties of waves characterized by a narrow band of frequencies and orientations. The narrow spectrum is centered around a peak frequency, wavenumber and wave orientation. Locally, the free surface elevation (measured with respect to the undisturbed water level $z = 0$) is described by:

$$\zeta = \frac{H}{2}\cos\Phi, \qquad \Phi = \kappa_x x + \kappa_y y - \omega t. \tag{1}$$

Here, Φ is the wave phase, whilst the wave height H is random and described by a Rayleigh distribution. Furthermore, $\kappa_x = -\kappa\cos\theta$ and $\kappa_y = \kappa\sin\theta$ are the x- and y-component of the wavevector $\vec{\kappa}$ and κ is the wavenumber. The peak frequency associated with the random wave field is ω and θ is the angle of wave incidence measured with respect to the shore-normal (clockwise deviation with respect to shore-normal means positive θ and vice versa, see Figure 2).The probability density distribution of values H' attained by the wave height reads

$$P(H') = \frac{2H'}{H_{rms}^2}\, e^{-(H'/H_{rms})^2}, \tag{2}$$

with H_{rms} the root-mean-square wave height. The energy $\mathcal{E}$ (per surface area) of a random wave field, apart from a factor ρg with g the gravitational acceleration and ρ the water density), is defined as

$$\mathcal{E} = \langle\zeta^2\rangle = \frac{1}{8}H_{rms}^2. \tag{3}$$

The brackets $\langle\ \rangle$ denote a time average over several wave periods and integration over all possible wave heights.

[14] Below, equations are discussed that govern the behavior of κ, θ, ω and $\mathcal{E}$, which are allowed to vary slowly in space. Here, we assume stationary wave conditions. The law of conservation of wave crests [*Mei et al.*, 2005, chapter 2] implies that the wave frequency ω is constant. The frequency of gravity waves is related to wavenumber κ by the dispersion relation

$$\omega^2 = g\kappa\tanh(\kappa D). \tag{4}$$

The wavenumber is the length of the wavevector, $\kappa = (\kappa_x^2 + \kappa_y^2)^{1/2}$, and D is the water depth (averaged over many waves). The angle of wave incidence is governed by the wavenumber identity relation:

$$\frac{\partial}{\partial y}(\kappa\cos\theta) + \frac{\partial}{\partial x}(\kappa\sin\theta) = 0. \tag{5}$$

Finally, the energy is controlled by the wave energy balance:

$$\vec{\nabla}\cdot\left(\vec{c}_g\mathcal{E}\right) = \mathcal{F} - \mathcal{D}. \tag{6}$$

Here, $\vec{\nabla}$ is the two-dimensional (horizontal) nabla vector with components $\frac{\partial}{\partial x}$ and $\frac{\partial}{\partial y}$ in the x- and y-direction, respectively. Furthermore, $\vec{c}_g$ is the group velocity vector of the waves with amplitude c_g and components $c_{gx} = -c_g\cos\theta$ and $c_{gy} = c_g\sin\theta$. Its magnitude c_g is

$$c_g = \frac{\partial\omega}{\partial\kappa} = \frac{\omega}{2\kappa}\left(1 + \frac{2\kappa D}{\sinh(2\kappa D)}\right). \tag{7}$$

The two terms on the right-hand side of equation (6) are the source of energy provided by wind forcing, $\mathcal{F}$, and the energy dissipation, $\mathcal{D}$, respectively. Dissipation can be the consequence of different processes, e.g., bottom friction, whitecapping and wave breaking. In the inner shelf region the dissipation is dominated by bottom friction. It is assumed that dissipation and generation of wave energy cancel on the outer shelf. The formulations for the
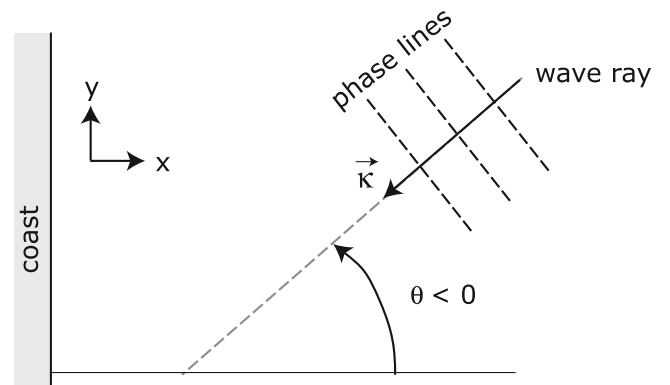

Figure 2. Definition of the angle of wave incidence θ. It is measured with respect to the shore-normal. Clockwise (anticlockwise) deviation with respect to the shore-normal means positive (negative) θ.

dissipation (adopted from *Komen et al.* [1994]) and generation of wave energy used in this study are:

$$\mathcal{D} = \frac{2c_f \kappa u_w \,\mathcal{E}}{\sinh(2\kappa D)}, \qquad \mathcal{F} = \mathcal{D}|_{x=L_s}. \qquad (8)$$

Here, c_f is a wave friction factor and

$$u_w = \frac{\omega H_{rms}}{2\sinh(\kappa D)} \qquad (9)$$

is the root-mean-square amplitude of the near-bed wave orbital motion.

2.2.2. Currents

[15] It is assumed that the large-scale water motion (i.e., that part of the water motion that remains after averaging over a number of waves) is governed by the depth- and wave-averaged (2DH) shallow water equations

$$\frac{\partial \vec{v}}{\partial t} + \left(\vec{v}\cdot\vec{\nabla}\right)\vec{v} + f\,\vec{e}_z \times \vec{v} = -g\vec{\nabla}z_s + \frac{\vec{\tau}_s - \vec{\tau}_b}{\rho D}, \qquad (10)$$

$$\frac{\partial D}{\partial t} + \vec{\nabla}\cdot(D\vec{v}) = 0. \qquad (11)$$

Here, $\vec{v}$ is the depth-averaged and wave-averaged velocity, f the Coriolis parameter, $\vec{e}_z$ is a unit vector in the vertical direction, z_s and z_b are the free surface elevation and the bottom depth both measured with respect to the undisturbed water level $z = 0$. Furthermore, the water depth $D = z_s - z_b$ and $\vec{\tau}_s$ and $\vec{\tau}_b$ represent the wind stress and bed shear-stress. In the momentum equations (10) forcing terms due to wave-induced radiation stresses, horizontal momentum diffusion, density gradients and tides are neglected. Furthermore, the rigid-lid approximation is used based on the small velocity of water particles with respect to the phase speed of gravity waves (small Froude number). As the free surface elevation is much smaller than the undisturbed water depth in this case, the local depth can be approximated by $D \simeq -z_b$. It is assumed that the mean storm-driven flow is in the alongshore direction (cross-shore component is neglected), which is driven by a prescribed wind stress τ_{sy}. During storms the amplitude of the wave orbital motion is much larger than the magnitude of the storm-induced current. Under wave-dominated conditions the mean bed shear-stress is linearly related to the mean flow. Assuming waves and currents to be near-parallel, it follows

$$\vec{\tau}_b = \rho r u_w \vec{v}, \qquad (12)$$

where u_w has been defined in section 2.2.1. The friction coefficient r computed for random waves is a factor $\sqrt{\pi}/2$ larger compared to the case of monochromatic waves considered in *Calvete et al.* [2001a]. Note that the mean bottom stress is related to the depth-averaged current rather than to the bottom velocity.

[16] The boundary conditions are that the cross-shore flow component u vanishes at $x = 0$ and far offshore. The bed level z_b has a fixed value at these two positions. As a consequence no net exchange of water occurs between the shoreface and inner shelf.

2.3. Sediment Transport

[17] Field observations by *Green et al.* [1995] show that during storms large amounts of sand are in suspension and transported without having any contact with the bed (suspended load transport). A smaller part of the grains moves within a thin layer close to the bed by rolling, sliding and hopping and is in frequent contact with the bed (bed load transport). *Calvete et al.* [2001a] argued that both types of transport must be included in the sediment transport formulation to correctly describe the growth and migration of sfcr. The total volumetric transport of sediment per unit width $\langle \vec{q}_t \rangle$ (averaged over several wave cycles) thus has two contributions:

$$\langle \vec{q}_t \rangle = \langle \vec{q}_b \rangle + \langle \vec{q}_s \rangle, \qquad (13)$$

where $\langle \vec{q}_b \rangle$ and $\langle \vec{q}_s \rangle$ represent the transport of sediment as bed load and suspended load, respectively. Formulations for these transports are given in section 2.3.1 and 2.3.2. As a simplification, the sediment is considered to be non-cohesive and of a single grain size.

2.3.1. Bed Load

[18] The formulation of *Bailard* [1981] is used to describe the bed load transport of sediment. For stormy weather conditions and waves propagating almost parallel to the storm-driven current, it follows

$$\langle \vec{q}_b \rangle = \begin{cases} \frac{3}{2}\nu_b \left(u_w^2 - u_c^2\right)\left(\vec{v} - \lambda_b u_w \vec{\nabla}z_b\right) & u_w^2 > u_c^2, \\ 0 & u_w^2 \le u_c^2. \end{cases} \qquad (14)$$

The coefficient ν_b depends on sediment properties and λ_b is the bed slope parameter which is related to the angle of repose of the sediment. Coefficient λ_b is a factor $3\sqrt{\pi}/4$ larger compared to the case of monochromatic waves. Furthermore, u_c is the critical wave orbital velocity amplitude above which erosion of sediment occurs. The first contribution to $\langle \vec{q}_b \rangle$ represents the net sediment transport due to a stirring of sediment by the waves and the subsequent transport by the net current. The second contribution accounts for gravitational effects on sediment grains in the bed load layer. Hereafter, the first contribution is called the current-induced sediment transport and the second the bed slope sediment transport. Bed load sediment transport only occurs if the shear-stress exerted on the bed exceeds a critical value.

2.3.2. Suspended Load

[19] The volumetric suspended load sediment transport per unit width, averaged over a large number of wave cycles, is a modified version of the suspended load transport proposed by *Bailard* [1981] and reads

$$\langle \vec{q}_s \rangle = \mathcal{C}\vec{v} - \lambda_s u_w^5 \,\vec{\nabla}z_b. \qquad (15)$$

Here, $\mathcal{C}$ is the depth-integrated relative volume concentration of sediment and λ_s is the bed slope parameter for suspended sediment. The latter is a factor $15\sqrt{\pi}/8$ larger compared to the case of monochromatic waves. A

formulation for the depth-integrated volume concentration (derived assuming a balance between the erosion and deposition flux near the bed) is adopted from *van Rijn* [1993] and also used by *Calvete et al.* [2001a]:

$$C = \delta D c_a, \qquad c_a = \begin{cases} \hat{c}_a \left(\frac{u_w^2 - u_c^2}{u_c^2} \right)^{3/2} & u_w^2 > u_c^2, \\ 0 & u_w^2 \le u_c^2. \end{cases} \quad (16)$$

Here, δ is the ratio of the thickness of the suspended load sediment layer and the actual water depth and c_a the reference volume concentration. The coefficient $\hat{c}_a$ is a constant and a factor $3\sqrt{\pi}/4$ larger compared to the case of monochromatic waves. As in the case of bed load, transport of suspended sediment only occurs if the shear-stress exerted on the bed exceeds a critical value leading to entrainment of sediment particles. The corresponding boundary condition is that the concentration vanishes far from the coast.

2.4. Bottom Evolution

[20] The evolution of the bottom is governed by:

$$(1-p)\frac{\partial z_b}{\partial t} + \vec{\nabla} \cdot \langle \vec{q}_b \rangle + \vec{\nabla} \cdot \langle \vec{q}_s \rangle = 0, \quad (17)$$

where $\langle \vec{q}_b \rangle$ and $\langle \vec{q}_s \rangle$ are given in equations (14) and (15). The porosity of the bed is indicated by p.

[21] Note that sfcr evolve on a timescale of decades to centuries, which is much longer than the daily to weekly variation of hydrodynamic processes. This allows use of the quasi-steady approximation: time derivatives in the hydrodynamic equations are neglected. Physically, this means that the water motion adjusts instantly to a new bed level.

3. Solution Method

[22] The initial growth of morphodynamic features is investigated by applying a linear stability analysis. The starting point is a longshore uniform basic state which describes an incoming wave field and a longshore storm-induced current. The inner shelf has a plane slope and bars are not yet present. The morphodynamic evolution of small perturbations in the basic state yields information about the growth or decay of features. As the focus is on the initial growth of bed features, the governing equations are linearized, which means that only terms that are proportional to the amplitude of the perturbations are retained. The linearization procedure is outlined in section 3.2. The result is an eigenproblem which is solved numerically using a spectral method. The solution for a fixed bed level gives the perturbed wave and velocity fields, which in turn are used to calculate changes in the bed level. From here on we denote solutions of primary wave variables by $\mathcal{X} = (\kappa, \theta, \mathcal{E})$ and those of other dependent variables by $\Psi = (u, v, z_s, \mathcal{C}, z_b)$.

3.1. Basic State

[23] It turns out that in case $H = H(x)$, as stated in section 2.1, the model allows for a basic state that is steady and alongshore uniform. Hence, $\mathcal{X} = \mathcal{X}_b(x)$ and $\Psi = \Psi_b(x)$, where we write $\mathcal{X}_b = (K, \Theta, E)$ and $\Psi_b = (U, V, \xi, C, -H)$. Thus K, Θ and E represent the basic state wavenumber,

angle of wave incidence and wave energy, respectively. Likewise, U, V, ξ, C and H represent the basic state cross-shore and longshore velocity component, free surface elevation, depth-integrated volume concentration and bottom elevation, respectively.

[24] Now substitute $\mathcal{X} = \mathcal{X}_b$ in equations (4)–(9). It follows, as ω is constant, that equation (4) relates the basic state wavenumber $K(x)$ to water depth $H(x)$. This relation is transcendental in K and can be solved using a root-finding procedure. Next, equation (5) reduces to $K \sin \Theta = $ constant, which is Snell's law. For a given angle of wave incidence $\Theta = \Theta_s$ on the outer shelf, it follows

$$\sin \Theta = \frac{K_s \sin \Theta_s}{K}. \quad (18)$$

Here, K_s is the wavenumber at $x = L_s$, which is known from the dispersion relation. The basic state wave energy $E(x)$ is governed by:

$$\frac{d}{dx}\left(-E \, C_g \cos \Theta \right) = \mathcal{F}_b - \mathcal{D}_b, \quad (19)$$

where C_g, $\mathcal{F}_b$ and $\mathcal{D}_b$ (thus U_w) are obtained from equations (7)–(9) by substitution of basic state variables. As boundary condition the wave energy $E = E_s$ (or equivalently, $H_{rms,s}$) on the outer shelf is prescribed. The basic state wave orbital velocity amplitude $U_w(x)$ is important for calculating the basic state flow and sediment transport.

[25] The basic state describes a longshore current with a cross-shore gradient, $\vec{v} = (0, V(x))$, which is driven by a constant alongshore wind stress τ_{sy}. The momentum equations for the basic state reduce to the following form:

$$fV = g\frac{d\xi}{dx}, \qquad 0 = \frac{\tau_{sy} - \tau_{by}}{\rho D}. \quad (20)$$

The first equation determines the cross-shore set-up or set-down of the water level due to Ekman effects. The second equation together with the rigid-lid approximation ($D = H$) and the linear friction law $\tau_{by} = \rho r U_w V$ determine the basic state alongshore velocity profile:

$$V = \frac{\tau_{sy}}{\rho r U_w}. \quad (21)$$

Note that the formulation for the alongshore velocity is only valid under wave-dominated conditions. The corresponding basic state depth-integrated relative volume concentration $C(x)$ follows from substitution of the basic state variables into equation (16)

$$C = \begin{cases} \delta H \hat{c}_a \left(\frac{U_w^2 - u_c^2}{u_c^2} \right)^{3/2} & U_w^2 > u_c^2, \\ 0 & U_w^2 \le u_c^2. \end{cases} \quad (22)$$

It is implicitly assumed that the basic state inner shelf equilibrium profile is due to the balance between downslope gravitational transport and onshore transport due to waves.

Therefore, the basic state defines a morphodynamic equilibrium. In this case the sediment and mass conservation equations are automatically obeyed.

3.2. Linear Stability Analysis

[26] The stability properties of the basic state are considered by studying the dynamics of small perturbations evolving on this basic state. Hence, $\mathcal{X} = \mathcal{X}_b + \mathcal{X}'$ is substituted in equations (4)–(9) and together with $\Psi = \Psi_b + \Psi'$ into equations (10)–(17). Both $\mathcal{X}_b$ and Ψ_b are defined in section 3.1. Furthermore, $\mathcal{X}'(x, y, t) = (\kappa', \theta', e')$ and $\Psi'(x, y, t) = (u', v', \eta', c', h')$ denote the perturbed variables, which are assumed to have small values with respect to their basic state values. To close the model, also perturbations in the group velocity, energy dissipation and wave orbital velocity need to be considered: $(c_g, \mathcal{D}, u_w) = (C_g, \mathcal{D}_b, U_w) + (c_g', \mathcal{D}', u_w')$. Expressions for $c_g', \mathcal{D}'$ and u_w' in terms of κ', θ', e' and h' readily follow from equations (7)–(9). As the morphodynamic patterns which are investigated are naturally confined to the inner shelf, appropriate offshore boundary conditions are $\mathcal{X}', \Psi' \rightarrow 0$ for $x \rightarrow \infty$. At the shoreface ($x = 0$) the boundary conditions are a vanishing cross-shore flow component ($u' = 0$) and a bottom elevation which is fixed to its basic state value ($h' = 0$). Linearizing the equations with respect to the small perturbed variables results in a linear system of differential equations. Note that use of the quasi-steady approximation implies that time derivatives of hydrodynamical variables are excluded. The system of perturbed equations sustains solutions which are periodic in the longshore direction and of which the amplitude can grow (or decay) exponentially in time:

$$
\begin{aligned}
&\left(\mathcal{X}', \Psi', c_g', \mathcal{D}', u_w'\right) \\
&= \mathcal{R}e\left\{\left(\hat{\chi}(x), \hat{\psi}(x), \hat{c}_g(x), \hat{\mathcal{D}}(x), \hat{u}_w(x)\right) e^{iky+\sigma t}\right\}.
\end{aligned}
\tag{23}
$$

Here, $\mathcal{R}e$ denotes the real part of the solution, k the longshore wavenumber (which can be assigned any value), the hats denote the as yet unknown cross-shore structure of the solutions and σ the complex frequency. Substituting expressions (23) into the equations for the small perturbations yields

$$
\hat{\kappa} = \left(\frac{K^2}{KH + \frac{1}{2}\sinh(2KH)}\right)\hat{h},
\tag{24a}
$$

$$
\begin{aligned}
&\frac{d}{dx}\left(K\cos\Theta\,\hat{\theta}\right) - ikK\sin\Theta\,\hat{\theta} \\
&= -\frac{d}{dx}(\sin\Theta\,\hat{\kappa}) - ik\cos\Theta\,\hat{\kappa},
\end{aligned}
\tag{24b}
$$

$$
\begin{aligned}
&\frac{d}{dx}\left(-C_g\cos\Theta\,\hat{e}\right) + ik\,C_g\sin\Theta\,\hat{e} \\
&= -\frac{d}{dx}\left(E\,\hat{c}_{gx}\right) - ik\,E\,\hat{c}_{gy} - \hat{\mathcal{D}}.
\end{aligned}
\tag{24c}
$$

Here, $\hat{c}_{gx} = (-\cos\Theta\,\hat{c}_g + C_g\sin\Theta\,\hat{\theta})$ and $\hat{c}_{gy} = (\sin\Theta\,\hat{c}_g + C_g\cos\Theta\,\hat{\theta})$ are the x- and y-component of the perturbed

group velocity, respectively. The expression for the cross-shore structure of the perturbed wave orbital velocity, which is e.g., used in calculating $\hat{\mathcal{D}}$, follows from equation (9):

$$
\hat{u}_w = U_w\left(\frac{\hat{e}}{2E} - \frac{H\hat{\kappa} - K\hat{h}}{\tanh(KH)}\right).
\tag{25}
$$

A similar procedure is followed for deriving the perturbed flow and sediment transport equations. These are almost identical to the equations obtained in the work of *Calvete et al.* [2001a], except that their parameterization (2.5) for u_w is not used and an extra friction term $-r\,V u_w'/H$ appears in the alongshore momentum balance. The latter is a consequence of the fact that the present study includes perturbations in the wave orbital velocity.

[27] The equations above, together with the corresponding boundary conditions which were specified before, define an eigenvalue problem

$$
\sigma\,\mathcal{S}\begin{bmatrix}\hat{\chi} \\ \hat{\psi}\end{bmatrix} = \mathcal{L}_k\begin{bmatrix}\hat{\chi} \\ \hat{\psi}\end{bmatrix},
\tag{26}
$$

where σ is the complex eigenvalue and $(\hat{\chi}, \hat{\psi})$ are the eigenfunctions. The latter ones give the cross-shore structure of the perturbations. The 8×8 matrix $\mathcal{S}$ contains the temporal information of the perturbations and all its elements are zeros, except for $\mathcal{S}(8,8) = 1$. Finally, the linear matrix operator $\mathcal{L}_k$ involves spatial derivatives and is therefore dependent on the longshore wavenumber k.

[28] The growth rate and migration speed of the perturbation is given by the complex frequency ($\sigma = \sigma_r + i\sigma_i$). The real part, σ_r, is the growth rate and the migration speed is given by $V_m = -\sigma_i/k$. If, for specific choices of the model parameters, $\sigma_r < 0$ for all k the basic state is stable. Conversely, if there is a range of wavenumbers k for which $\sigma_r > 0$, there are exponentially growing modes and the basic state is unstable. The mode which has the largest growth rate is called the fastest growing or most preferred mode. The basic idea of a linear stability analysis is that, starting from some random perturbation (which contains all Fourier modes), the fastest growing mode will dominate the solution after some time. The inverse of the growth rate σ_r gives a characteristic timescale for the formation in nature (called the e-folding growth time T_g). The eigenvalue problem is solved numerically using a spectral collocation method. Thus, variables are expanded in Chebyshev polynomials and equations are evaluated at N collocation points (see *Boyd* [2001] for details).

4. Results

4.1. Parameter Values: Default Case

[29] In this section results of the model are presented for a specific setting of the reference topography and for values of the parameters which are representative for the microtidal inner shelf of Long Island. It is situated at the Atlantic coast of North America near New York at a latitude of 40°. Several studies [cf. *Swift and Field*, 1981] have indicated the presence of large-scale bed forms in this area. The reference bottom profile, defined as the longshore- and time-averaged
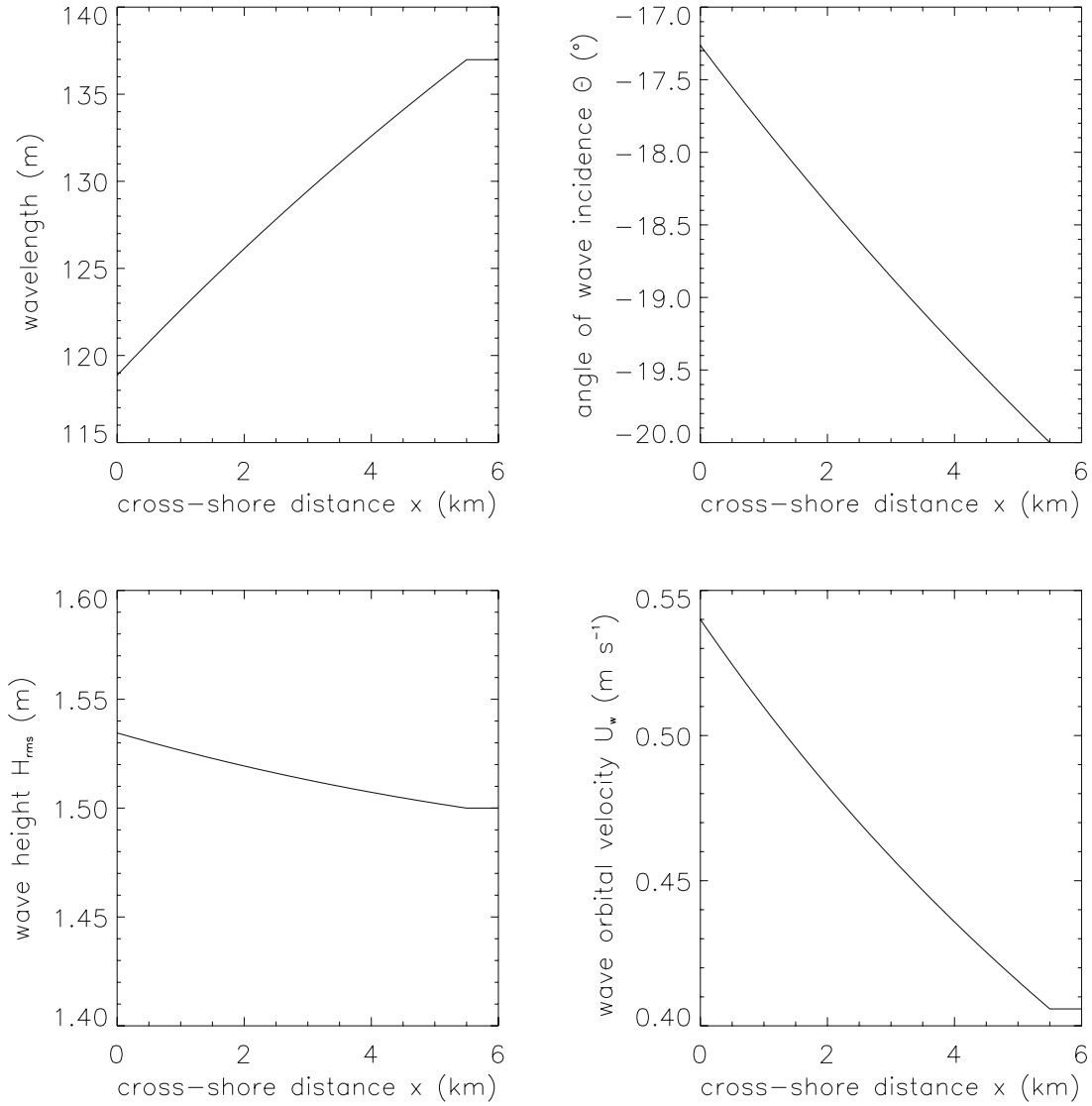
Figure 3. Basic state; cross-shore profiles of wavelength, angle of wave incidence, wave height and wave orbital velocity. Default case.

bottom profile of the continental shelf, is modeled as $z = -H(x)$, where

$$H(x) = \begin{cases} H_0 + \beta x & 0 \leq x \leq L_s, \\ H_s & x > L_s. \end{cases} \qquad (27)$$

Representative values for the geometrical parameters are $H_0 = 14$ m, $H_s = 20$ m and $L_s = 5.5$ km, hence the bottom slope $\beta = (H_s - H_0)/L_s \sim 1 \times 10^{-3}$. The Coriolis parameter at this location is $f = 1 \times 10^{-4}$ s^{-1}.

[30] Observations by *Niedoroda and Swift* [1981] and *Lentz et al.* [1999] indicate the importance of northeastern storms for the wave climate near Long Island. A typical value for the root-mean-square wave height on the outer shelf of Long Island is $H_{rms,s} = 1.5$ m. Note that the significant wave height, which is used in many studies, is a factor $\sqrt{2}$ larger. The waves approach from the northeast and the angle of wave incidence $\Theta_s = -20°$ (counter clockwise, with respect to the shore normal) when entering

the inner shelf. As we assume a stationary wave field, the wave frequency is constant. A typical value for the wave period is $T = 11$ s, so a wave frequency $\omega \sim 0.6$ s^{-1}. A wave friction factor $c_f = 3.5 \times 10^{-3}$ is used for determining dissipation of wave energy. For calculating the bottom shear-stress experienced by the current a friction coefficient $r = 2.0 \times 10^{-3}$ is used.

[31] The wind associated with the northeastern storms exerts a stress on the water surface which forces an alongshore current. Based on the field data discussed above the alongshore wind stress is chosen as $\tau_{sy} = -0.4$ N m^{-2} (southward). The alongshore current V is established as a balance between the storm-induced wind stress and the bottom stress. Note that the latter depends on the wave orbital velocity (see equation (21)). It is further assumed that grain size $d_{50} = 0.35$ mm, porosity $p = 0.4$, bed load parameter $\nu_b = 5.6 \times 10^{-5}$ s^2 m^{-1}, suspended load parameter $\hat{c}_a = 1.2 \times 10^{-5}$, critical velocity for erosion $u_c = 0.25$ m s^{-1} and bed slope parameters $\lambda_b = 0.65$ and $\lambda_s = 7.5 \times 10^{-4}$ s^4 m^{-3} (see equations (14)–(17)). Field data
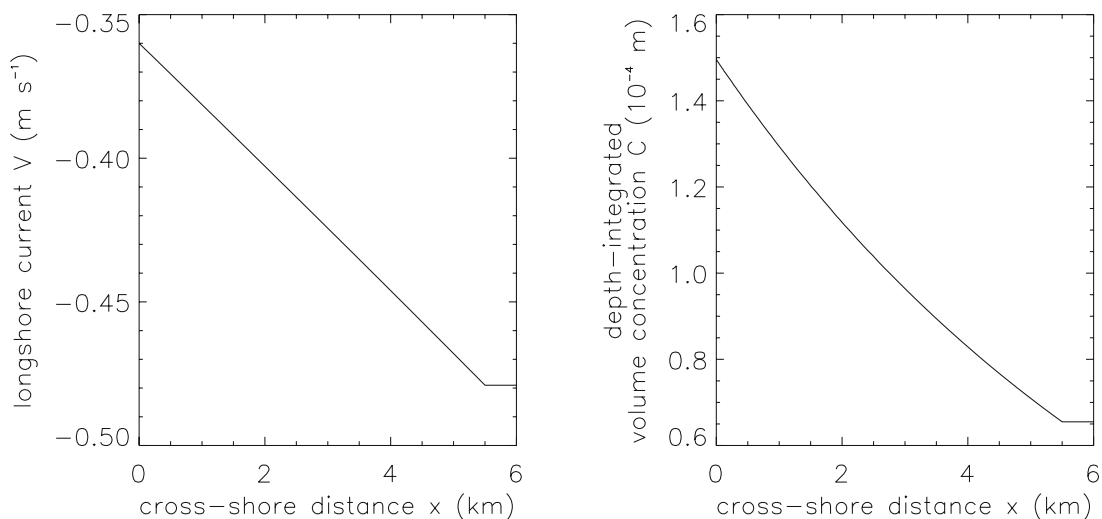
Figure 4. Basic state; cross-shore profiles of longshore current and depth-integrated volume concentration. Default case.

[*Williams et al.*, 1999] indicate that $\delta \sim 0.2$ for strong waves superimposed on a mean current. Values are similar to those proposed by *Calvete et al.* [2001a].

[32] The cross-shore profiles for the basic state wave variables are shown in Figure 3. A decrease in water depth causes a shortening and refraction of the waves. Wave height increases towards the shore due to decreasing group velocity. As a result, the amplitude of the near-bed wave orbital velocity also increases into shallower depths and reaches an amplitude of 0.54 m s^{-1} at the shoreface.

[33] The cross-shore profiles of the basic state longshore current and depth-integrated concentration are shown in Figure 4. The magnitude of the longshore current decreases towards the shoreface, reaching a value of 0.36 m s^{-1}. This is a consequence of the larger bottom friction for shallower depths. The depth-integrated concentration of sediment increases towards the shoreface as the larger wave orbital motion stirs more sediment into suspension.

4.2. Linear Stability Analysis: Default Case

[34] The growth rate of small perturbations evolving on the basic state of the model as a function of their longshore wavenumber k is displayed in Figure 5a. In the calculations it is assumed that growth of the perturbations takes only place during storms, which occur during a time fraction of 5%. Model output is corrected for this. For this default case
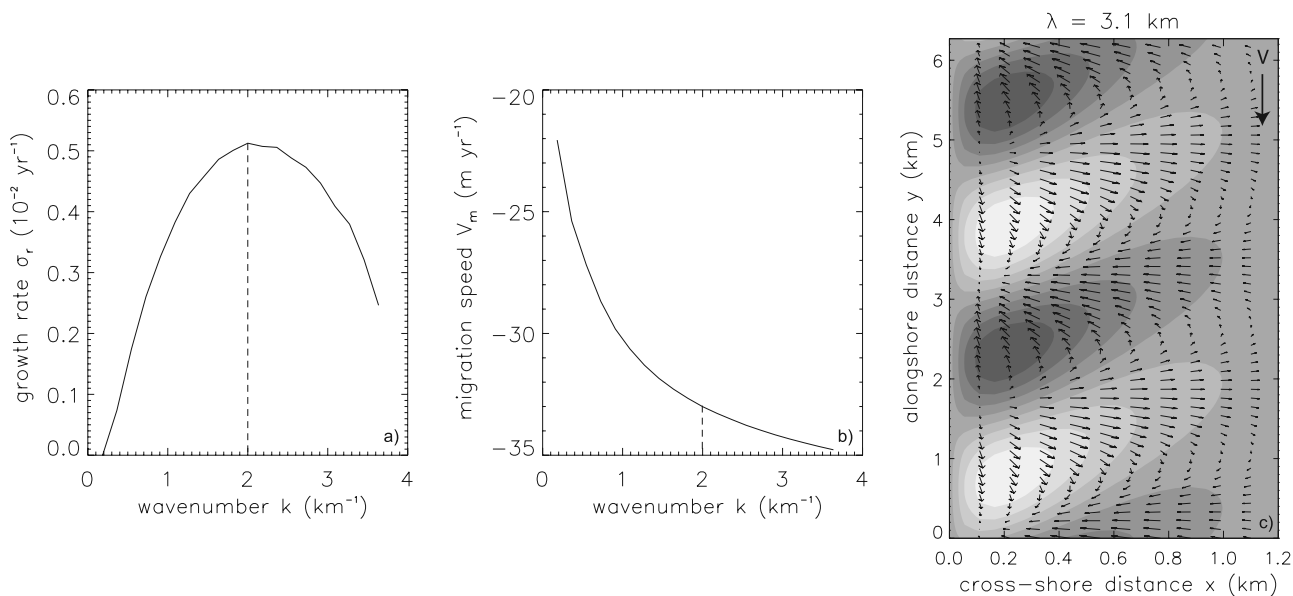

Figure 5. Growth rates (a) and migration velocities (b) as a function of the longshore wavenumber. The dashed lines indicate the most preferred mode. (c) Bottom perturbations (greyscale; light: bars, dark: troughs) and perturbations (small arrows) in basic longshore velocity field (in direction of thick arrow) for the maximum in the growth rate curve. The aspect ratio has been increased to show the arrows.
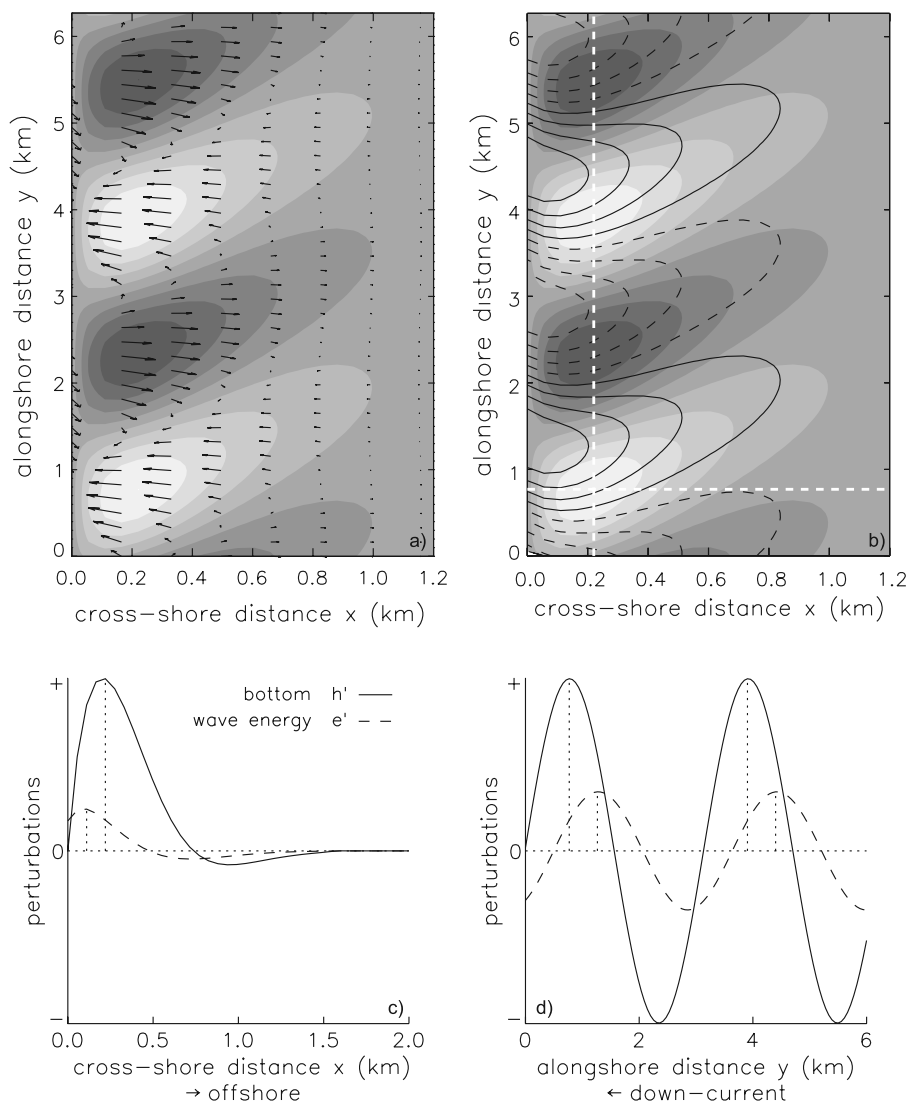
Figure 6. (a) Spatial structure of the perturbed bottom (greyscale; light: bars, dark: troughs) and of the perturbed wavevector (small arrows); the fastest growing mode. The aspect ratio has been increased to show the arrows. (b) Bottom pattern of the most preferred mode (greyscale; light: bars, dark: troughs) and spatial distribution of the perturbed wave energy (contours; solid: $e' > 0$, dashed: $e' < 0$). The dashed white lines indicate the position of normal and longshore cross-sections through the ridges, which are shown in (c) and (d), respectively.

one growing solution is obtained. The dashed line indicates the wavenumber $k = k_p$ of the most preferred mode, which has the largest growth rate. Here $k_p \sim 2.0$ km^{-1}, which corresponds to a longshore wavelength of the bed forms of $\lambda = 2\pi k^{-1} \sim 3.1$ km. It follows from Figure 5b that the preferred mode migrates approximately 33 m yr^{-1} in the downstream direction.

[35] The bottom pattern of this preferred bed form is shown in Figure 5c. The light areas denote the crests and the dark areas the troughs. Clearly, sfcr are found with seaward ends of the ridges rotated up-current with respect to the shoreface attachments. The angle between the crest axis and the coastline (from here on denoted as φ) is about 30°. The ridges extend up to 1 km in offshore direction. The thin arrows denote the flow perturbation and show an offshore (onshore) current deflection over the crests (troughs) of the

bars. The e-folding timescale for the growth of the ridges $T_g = \sigma_r^{-1} \sim 195$ yr.

[36] In Figure 6a both the bottom pattern of the preferred mode (greyscale) and perturbations in the wavevector (small arrows) are shown. A significant convergence of wave rays is visible at the upstream side of the ridges, which is due to bed form-induced wave refraction. The focusing of waves in the upstream region causes an increase in wave energy, which is clearly visible in Figure 6b. The shore-normal (Figure 6c) and longshore (Figure 6d) cross-sections at the positions of the dashed lines show that perturbations in wave energy are located up-current and onshore with respect to the bottom perturbations.

[37] In Figure 7a the spatial distribution of the perturbed wave orbital velocity and bottom of the most preferred
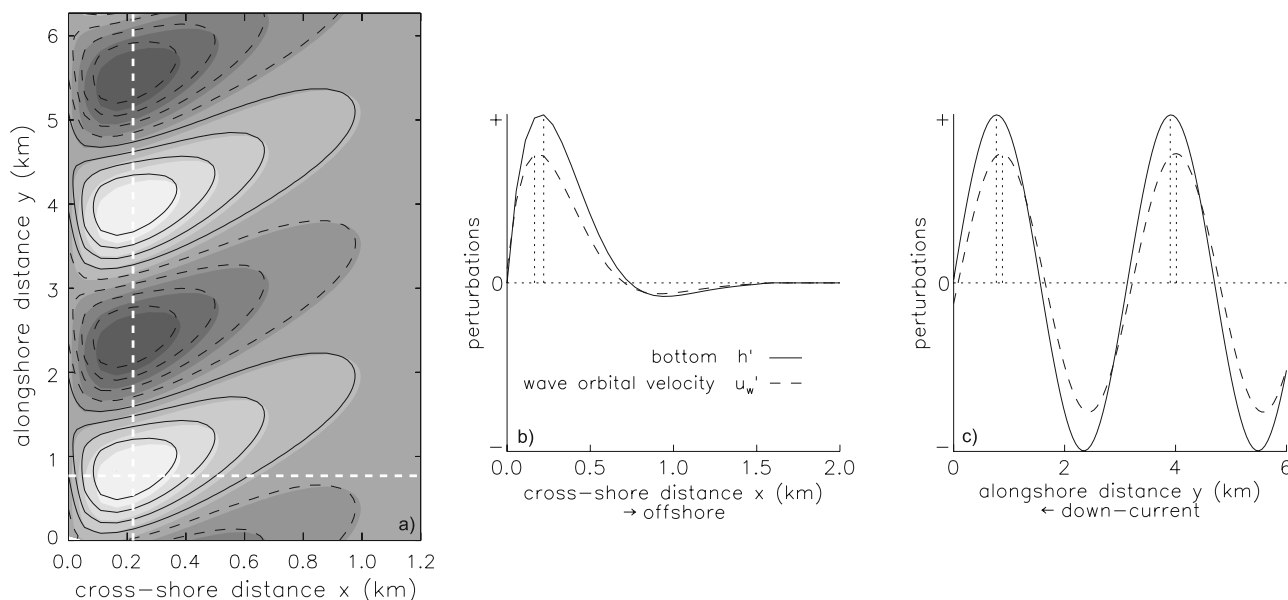
Figure 7. (a) Bottom pattern of the most preferred mode (greyscale; light:bars, dark:troughs) and spatial distribution of the perturbed wave orbital velocity (contours; solid: $u'_w > 0$, dashed: $u'_w < 0$). The dashed white lines indicate the position of normal and longshore cross-sections through the ridges, which are shown in (b) and (c), respectively.

mode are shown. A small phase shift in the cross-shore direction exists (see Figure 7b). The longshore cross-section along the vertical white dashed line (Figure 7c) reveals that the pattern of the wave orbital velocity is shifted up-current with respect to that of the bottom. As will be demonstrated later on, this phase shift between the perturbed wave orbital velocity amplitude and the perturbed bottom is crucial to understand the growth of bed forms due to their feedback with the waves.

[38] Focusing of wave energy in areas upstream of the ridges causes an enhanced entrainment of sediment in these areas and therefore an increase in depth-integrated sediment concentration (results not shown).

4.3. Sensitivity to the Wave-Bed Form Feedback Mechanism

[39] In this section the effect of wave-topography interactions on growth, migration and spatial characteristics of ridges is investigated. This is done by excluding perturbations in the wave orbital motion: $u'_w = 0$, hence $u_w = U_w$. Physically, this means that wave refraction and shoaling and dissipation of wave energy due to the presence of bed forms are neglected together with the friction term related to perturbations in the wave orbital velocity. Note that the latter was assumed in all previous models for sfcr, although a basic state wave orbital velocity was parametrically described. Default values for the parameters were used.

[40] Results (not shown) reveal that the basic state is stable with respect to perturbations having a wavenumber $k > 2.2$ km^{-1}. For smaller wavenumbers two modes are found with positive growth rates. The first mode has a maximum growth rate for a wavelength $\lambda = 6.9$ km, whereas the second mode attains its maximum for $\lambda = 4.9$ km. The growth rates are positive, but very small: e-folding time-

scales are $\sim 10^4$ yr. Their migration speeds are ~ 0.7 m yr^{-1} in the direction of the longshore basic current.

[41] The bottom pattern of both modes consists of up-current oriented ridges which span the whole width of the inner shelf. The angle between crest axis and coastline is $\varphi \sim 30°$ for the first mode and $\varphi \sim 25°$ for the second mode.

4.4. Sensitivity to the Reference Bottom Slope

[42] Previous models [cf. *Trowbridge*, 1995] indicated that the growth of ridges decreases monotonically with decreasing transverse bed slopes and no growth occurs in case that $\beta = 0$. However, these models did not account for perturbations in the wave orbital velocity. Therefore, we investigated the sensitivity of the growth process to the transverse bottom slope with the new model. Experiments were performed using default parameter settings, except for changing the water depth at the outer shelf H_s (and thus the transverse bed slope). The slope was gradually increased from 0 to the default value of 1×10^{-3}.

[43] Already in case of a horizontal bottom growing perturbations are obtained. The fastest growing mode has an e-folding time of 249 yr. The most preferred alongshore spacing is 2.7 km. The bed forms are closely confined to the shoreface, up-current oriented and they migrate with 35 m yr^{-1} in the down-current direction. They span only about 15% (up to 0.8 km) of the inner shelf width. The obliqueness of the crest axis with respect to the coastline is somewhat larger than 35°. Slowly increasing the transverse bottom slope to the default value results in a slightly larger longshore spacing, 25% increase in growth rate and a minor decrease in migration speed. The offshore extent of the ridges increases from 0.8 km (zero slope) to 1.0 km (default slope).
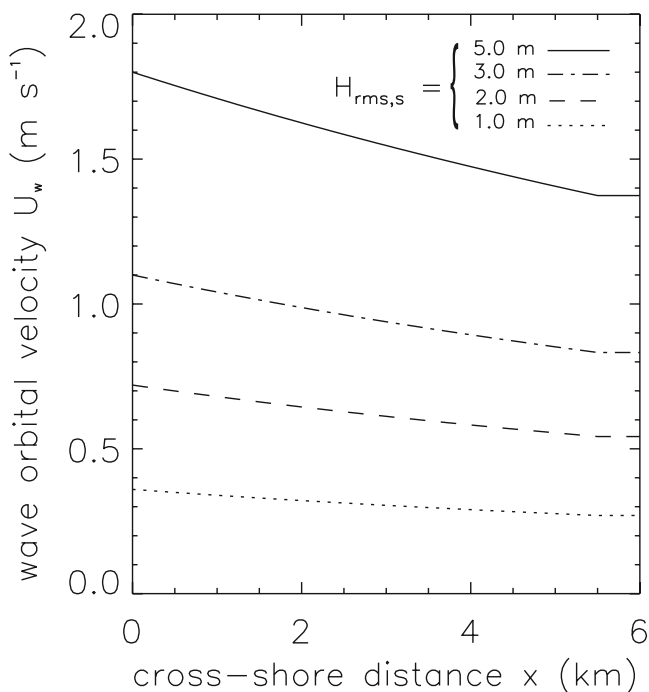
Figure 8. Cross-shore profiles of the wave orbital velocity amplitude in the basic state for different offshore wave heights.

4.5. Sensitivity to Model Parameters

[44] One noticeable new element in the present study is the incorporation of a wave module based on physical principles. Consequently, it is important to investigate the dependence of model results on three new parameters viz., wave height, wave period and the angle of wave incidence at the offshore boundary $x = L_s$. For all sensitivity experiments that will be discussed below default values for the parameters were used, unless mentioned otherwise. A range of conditions was examined. The offshore wave height $H_{rms,s}$ was varied between 1.0 and 5.0 m representing a calm to a rough sea. The wave period T was varied such that both wind and swell seas are examined: $4 - 14$ s. The offshore angle of wave incidence Θ_s was varied between $-2°$ and $-50°$ (from the northeast), which covers the range of conditions observed. According to *Draper* [1991] wave height and wave period are related, i.e., the higher the wave, the larger the wave period. Therefore, some extra experiments were performed in which wave height and wave period were varied according to Draper's formulation. A few additional experiments were carried out to investigate the effect of wave dissipation and a critical velocity for erosion on the results.

4.5.1. Varying Wave Height

[45] For each of the different wave heights the basic state is computed and subsequently the stability problem is solved. Figure 8 shows results for the magnitude of the basic state wave orbital motion as a function of offshore wave height. As can be seen, waves with larger offshore wave height have a larger wave orbital velocity on the outer shelf. The higher the waves, the stronger their shoaling towards the coast which results in a stronger increase of

wave orbital velocities. The amplitude of the basic state longshore current is inversely related to the amplitude of the wave orbital motion. Therefore, in case of a rough sea the longshore current is relatively weak on the outer shelf and it decreases comparatively fast towards the shoreface. For the depth-integrated sediment concentration the opposite holds (but more strongly), as the latter is related to the third power of the wave orbital velocity.

[46] Performing the linear stability analysis for different offshore wave heights revealed that the system exhibits one growing mode in all cases. Figure 9 shows the preferred wavelength, e-folding growth time and migration speed as a function of the offshore wave height. In all cases the waves were assumed to be present during 5% of the time.

[47] The alongshore spacing between two successive crests increases from $\lambda = 3.5 \pm 0.3$ km for $H_{rms,s} = 1.0$ m to $\lambda = 11.5 \pm 0.3$ km for $H_{rms,s} = 5.0$ m. The e-folding growth time decreases rapidly with increasing offshore wave height, which indicates an increase in growth rate with a factor 13. Even more remarkable is the strong increase in migration speed from 10 m yr^{-1} for a wave height of 1.0 m to 300 m yr^{-1} for a wave height of 5.0 m, both still in the down-current direction. Note however that for 5.0 m high waves the assumed time fraction of occurrence should probably be a factor 10 smaller and corresponding values for growth time and migration speed would be 590 years and 30 m yr^{-1}, respectively. The results of experiments with wave heights and periods related as for the *Draper* [1991] formula (results not shown) indicate that precise knowledge about both wave height and wave period is crucial for obtaining accurate estimates of e-folding growth times. Differences between the default case and the Draper cases are most significant for smaller wave heights.

[48] The increase in alongshore spacing of the bed forms for higher offshore waves is accompanied by an increase in their cross-shore extent. This is clearly visible when Figure 10a, which displays the spatial structure of the most preferred mode for a wave height of 5.0 m, is compared with Figure 5c. For a wave height of 5.0 m the bed forms extend offshore to approximately 100% of the inner shelf width, instead of about 18% for the default case. The obliqueness of the ridge axis with respect to the coastline increases from $\varphi \sim 25°$ ($H_{rms,s} = 1.0$ m) to $\varphi \sim 35°$ ($H_{rms,s} = 5.0$ m).

[49] Another important feature is visible in Figures 10b and 10c, which show the perturbations in the wave orbital velocity and the bottom perturbations at a specific normal and alongshore transect through the ridges. For small wave heights the perturbed wave orbital velocity attains its maximum almost at the same offshore position as the ridge crest. However, faced in the longshore direction, the perturbation in the wave orbital velocity is slightly shifted up-current with respect to the bar position. When wave heights are increased the up-current phase shift in the along-shore direction between u'_w and h' increases significantly (Figure 10c). Furthermore, a clear cross-shore phase shift is formed, where the perturbed wave orbital velocity is shifted onshore with respect to the bottom perturbation (Figure 10b).

4.5.2. Varying Wave Period

[50] Similarly as before, the basic state is computed for different wave periods. Results reveal that the basic state
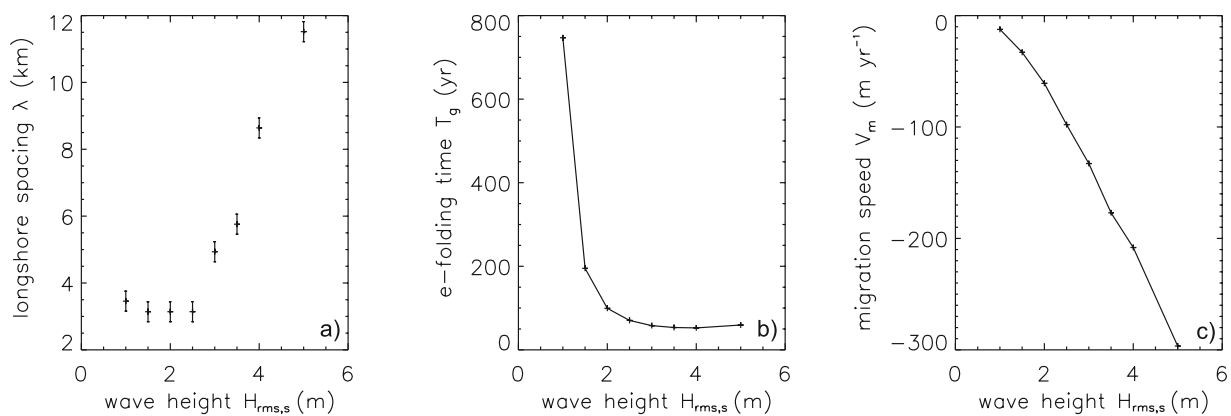
Figure 9. The sensitivity of the longshore spacing (a), e-folding growth time (b) and migration speed (c) of the fastest growing mode for the wave height at the outer shelf. Other parameters have their default values. The uncertainty in longshore spacing is indicated with the error bars. Uncertainties in e-folding time and migration speed are very small, so no error bars are shown.

wave orbital velocity amplitude is larger for low-frequency waves. This can be understood by realizing that two processes are competing here. The first is covered by the dispersion relation which shows a more than linear decrease in wavenumber with decreasing wave frequency. The indirect effect is an increase of the wave orbital velocity. The second effect is the direct reduction of the wave orbital velocity for lower wave frequencies. The competition is such that the indirect effect wins and wave orbital velocities increase for larger wave periods. As a consequence of the latter, the total sediment concentration in the water column will increase, whilst the basic state amplitude of the longshore velocity will decrease for waves with lower frequencies.

[51] The performed stability analysis indicates that one growing solution is obtained as long as the wave period exceeds 6 s. Figure 11 shows the preferred wavelength, e-folding growth time and migration speed for this mode as a function of the wave period.
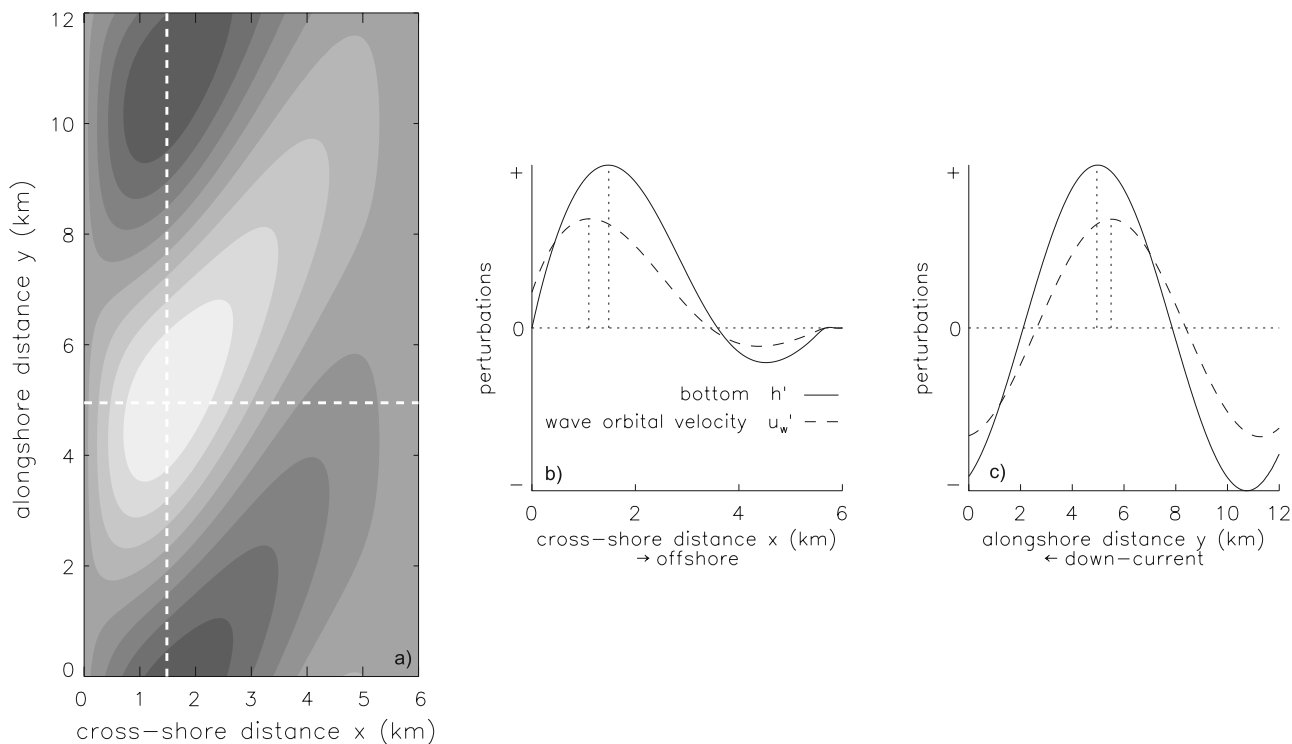

Figure 10. (a) Bottom pattern (greyscale; light: bars, dark: troughs) of the most preferred mode for a wave height of 5.0 m. The dashed white lines indicate the position of normal and longshore cross-sections through the ridges, which are shown in (b) and (c), respectively.
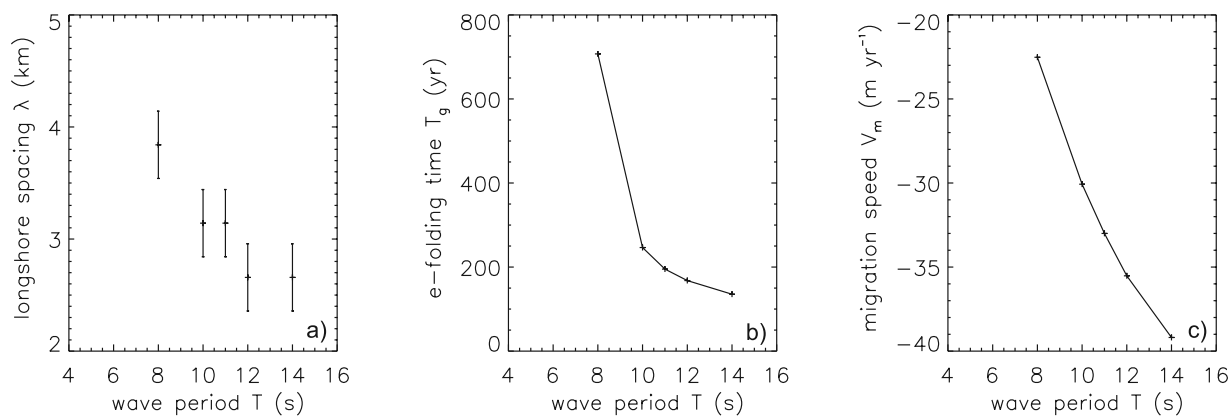
Figure 11. As Figure 9, but sensitivity for a change in wave period.

[52] The longshore spacing of the bed forms slightly decreases with an increase in wave period, but it saturates at a value of $\lambda = 2.7 \pm 0.3$ km. The e-folding growth time decreases with a factor 5, where the largest decrease takes place at lower wave periods. The migration speed of the ridges increases more or less linearly with increasing wave period and in all cases the ridges propagate downstream. The spatial structure of the bed forms is similar to the ones shown in Figure 5c. The crests reach up to 1 km offshore in all the experiments. The angle between crest axis and coastline ranges from $\varphi \sim 25°$ to $35°$, being the largest for low-frequency waves. Investigation of the phase shift between perturbed wave orbital velocities and bottom perturbations has shown an increase in the longshore phase shift for larger wave periods. For both low- and high-frequency waves the cross-shore maximum in the perturbed wave orbital velocity is exactly on top of the ridge and no phase shift exists.

4.5.3. Varying Angle of Wave Incidence

[53] The basic state is computed for varying offshore angles of wave incidence. The differences between the magnitude of basic state variables for all the experiments are small. In case of more oblique incident waves the wave orbital velocity and depth-integrated concentration of sediment become smaller and the current amplitude becomes larger.

[54] The linear stability analysis for distinct offshore angles of wave incidence provided clear mutual differences regarding the preferred wavelength, e-folding growth time and migration speed (Figure 12) of the most preferred mode. For angles of wave incidence $|\Theta_s| > 30°$ no clear maximum in the growth rate curve was found and thus no information is provided concerning the preferred wavelength of the evolving bottom patterns. For these specific experiments, the most preferred wavelength is estimated using the wavenumber at which the growth rate curve starts to saturate.

[55] For an angle of wave incidence almost normal to the shore at the outer shelf, the longshore spacing between successive crest is $\sim$5 km. Increasing the offshore angle of wave incidence to $-50°$ leads to a reduction in this spacing of at least 3 km. A similar behavior is observed for the offshore distance to which the ridges extend. The latter decreases from $\sim$1.5 km (about 30% of the inner shelf width) to $\sim$0.5 km (10% of the shelf width). The angle between ridge axis and coastline increases from about 25° to 30° for a change in the offshore angle of wave incidence from $-2°$ to $-20°$. For $|\Theta_s| > 20°$ the angle between ridge axis and coastline is independent of the offshore angle of wave incidence. More oblique incident waves favor a faster development of bottom patterns. The e-folding growth time decreases with about a factor 50 for very oblique incident waves with respect to near-normal incident waves. The
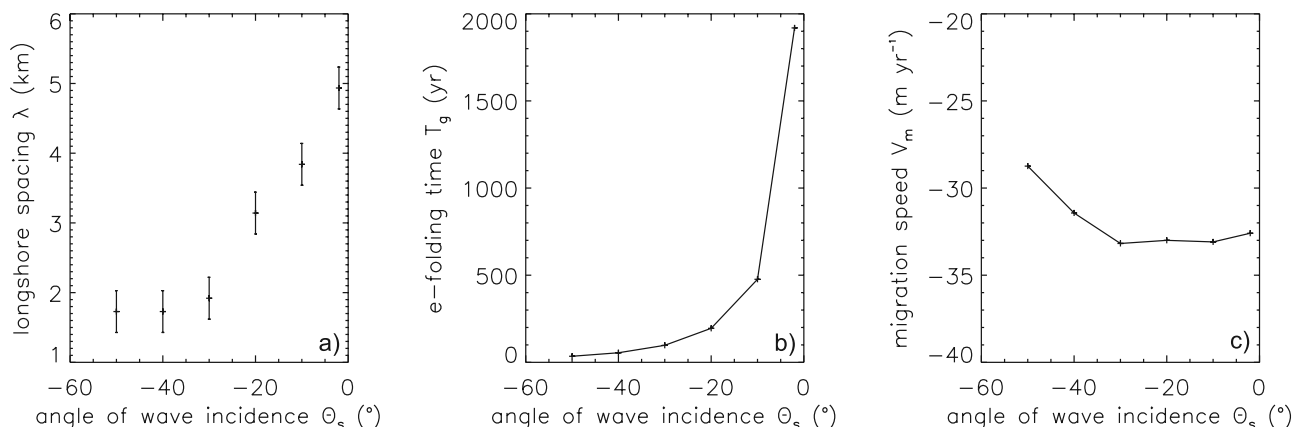

Figure 12. As Figure 9, but sensitivity for a change in angle of wave incidence at the outer shelf.

sensitivity of the bed form propagation speed to the offshore angle of wave incidence is limited. Enlarging the offshore angle of wave incidence from $-2°$ to $-50°$ results at first in a small increase in down-current migration speed, but in the end a decrease to about -29 m yr^{-1}. For angles of wave incidence which are sufficiently large, also a secondary and tertiary mode emerges.

4.5.4. Role of Other Processes

[56] So far we have presented results for cases in which the influences of both dissipation of wave energy and a threshold velocity for erosion are taken into account. The latter is a new element with respect to former studies, whereas dissipation is new in the sense that wave processes are explicitly described in this study. Experiments reveal that the above-mentioned processes are responsible for a 16% reduction in growth rates and a 13% decrease in propagation speeds. Critical shear-stresses for erosion contribute most significantly to the damping of growth and migration. The longshore spacing of bed forms is not affected by the two processes.

[57] Finally, the relative importance of bed load and suspended load transport in the default case is determined. Simulations show that 87% of bed form growth and migration are caused by suspended load transport.

5. Discussion

5.1. Physical Interpretation

[58] For the default setting of the model parameters, it has been demonstrated that the basic state is unstable and growing bottom perturbations resemble up-current oriented sfcr. In this section the physical processes responsible for the growth, migration and spatial pattern of these ridges are analyzed. A convenient procedure, which was also used by *Trowbridge* [1995] and *Calvete et al.* [2001a], is to derive an equation which combines the continuity equation for water (11) and the conservation equation for sediment mass (17). Linearizing both equations with respect to small perturbations and combining the results yields the so-called bed evolution equation

$$
\overbrace{(1-p)\frac{\partial h'}{\partial t}}^{T0} + \overbrace{\frac{3}{2}\frac{\nu_b U_w^2 V}{H}\frac{\partial h'}{\partial y}}^{T1} - \overbrace{\vec{\nabla}\cdot\left(\lambda_{bs}\vec{\nabla}h'\right)}^{T2}
$$
$$
= -\overbrace{\frac{d}{dx}\left(\frac{3}{2}\frac{\nu_b U_w^2}{H}\right)Hu'}^{T3} - \overbrace{\delta\frac{dC_a}{dx}Hu'}^{T4} \tag{28}
$$
$$
- \overbrace{\frac{\partial}{\partial y}\left(3\nu_b U_w V u_w'\right)}^{T5} - \overbrace{\frac{\partial}{\partial y}\left(\delta V H c_a'\right)}^{T6},
$$

where $\lambda_{bs} = (3/2)\,\nu_b\lambda_b U_w^3 + \lambda_s U_w^5$. The formulation is as in section 3 before substituting the longshore periodic and exponentially growing solutions. Here, in case of wave orbital velocities exceeding the critical velocity for erosion, the effects of the latter are ignored. Thus, the basic state reference volume concentration is written as $C_a = \hat{c}_a\,U_w^3/u_c^3$ for $U_w^2 > u_c^2$ (derived from equation (16) by substitution of basic state variables). By straightforward calculations it follows that the perturbed reference volume concentration is $c_a' = 3\hat{c}_a U_w^2 u_w'/u_c^3$.

[59] In the bed evolution equation, term T0 represents the growth or decay of bed forms. Bed forms grow (decay) if $\partial h'/\partial t > 0$ ($\partial h'/\partial t < 0$) above the crests. Term T1 describes the alongshore migration of the bed perturbations due to bed load processes. Term T2 is a consequence of the downslope sediment transport and causes diffusion of bed forms. The terms on the right-hand side of the bed evolution equation are possible sources of instabilities. Term T3 represents the *Trowbridge* [1995] mechanism in the specific case of $(3/2)\nu_b U_w^2 \rightarrow K = $ constant, in which K is called the sediment load. Essential for this mechanism to work is the presence of a transversely sloping reference bottom. Trowbridge demonstrated that in order to have growth, the current should exhibit an offshore deflection over the ridge. In other words, there must be a positive correlation between u' and h'. The latter only occurs if the ridges are up-current oriented. In addition, taking into account both term T3 and T4 of equation (28) gives the mechanism proposed by *Calvete et al.* [2001a]. They found that in order to have growth of up-current oriented ridges, the cross-shore gradient in the reference volume concentration (dC_a/dx) should be negative above ridge crests. Thus, the basic state wave orbital velocity U_w should increase towards the shoreface. Again, essential is the presence of an inner shelf with transverse bottom slope.

[60] Finally, terms T5 and T6 in the bed evolution equation are a consequence of bed form-induced perturbations in the wave orbital velocity u_w' and reference volume concentration c_a', respectively. These terms, of which term T6 is the dominant one, describe a new physical mechanism which is hereafter called the wave-bed form feedback mechanism. The latter is, in contrast with the other two mechanisms, also effective in case of a non-sloping reference bottom. In order to have a positive feedback between waves and bed forms term T6 (the dominant one) should be negative above a ridge and thus $\partial c_a'/\partial y > 0$ (note that V is negative). As c_a' is linearly related to u_w', this means that $\partial u_w'/\partial y > 0$ at the crests. More precisely, in order to have growth the spatial correlation $\overline{h'\left(\partial u_w'/\partial y\right)}$ should be positive, where the bar denotes averaging over the domain. Assuming $h' = \hat{h}(x)\cos(ky)$ and $u_w' = \hat{u}_w(x)\cos(ky - \phi(x))$, where ϕ denotes an alongshore phase shift between u_w' and h', it follows

$$
\overline{h'\frac{\partial u_w'}{\partial y}} \sim k\int_0^\infty \sin\phi\,\hat{h}\,\hat{u}_w\,dx. \tag{29}
$$

From this we see that a positive phase shift ϕ between $\hat{u}_w$ and $\hat{h}$ can initiate growth of bed forms and therefore the maximum in the perturbed wave orbital velocity should be located upstream of the maximum in the bed perturbation. This is only the case for up-current rotated ridges, which exhibit a clear convergence of perturbed wave energy at their upstream side (see Figures 6b–6d) with a corresponding increase in the magnitude of the wave orbital velocity (see Figure 7). Thus, the enhanced stirring of sediment by the waves in the upstream region causes an increase in the sediment concentration, which is subsequently transported by the background current and deposited at the downstream side of the ridges. The wave-bed form feedback mechanism thus leads to enhanced growth and migration of the bed forms.
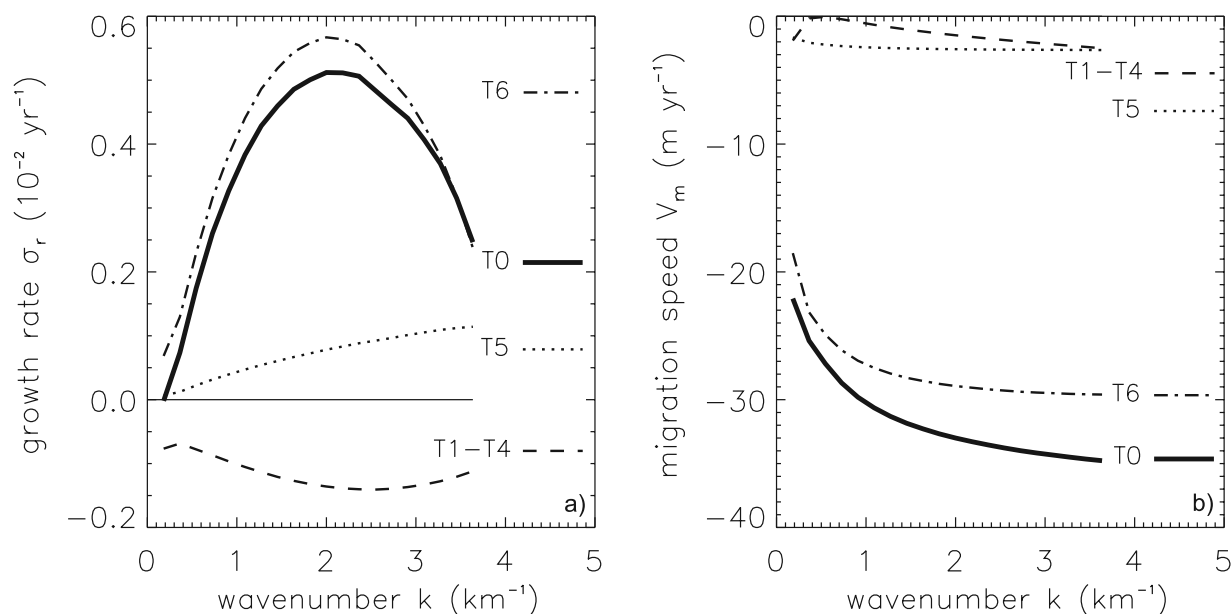
Figure 13. Relative contribution of the different terms in equation (28) to the growth rate (a) and migration speed (b) of the mode for the default case shown in Figure 5. Here, T0 is total and T1−T4 means T1 + T2 + T3 + T4.

[61] Similar derivations for the *Trowbridge* [1995] and *Calvete et al.* [2001a] mechanisms show that a phase shift between the cross-shore velocity perturbation (u') and the bed perturbation (h') can also initiate growth. However, the growth according to the wave-bed form feedback mechanism is linearly related to the alongshore wavenumber k (because of the longshore derivative $\partial u'_w/\partial y$), whereas the other two mechanisms are not. Consequently, the wave-bed form feedback mechanism dominates over the two other mechanisms, albeit that the latter are still significant. This is clearly visible in Figure 13 which shows, for the default case in Figure 5, the relative contributions of the different terms in equation (28) to total growth and migration.

[62] Analysis of equations (24b) and (24c) shows that the phase shift between wave orbital velocity perturbations and the bed topography is mainly a consequence of bed form-induced wave refraction. The latter is controlled by the second term on the left-hand side of the 'generalized Snell's law' (24b). The focusing of wave energy due to wave refraction is governed by the first two terms on the right-hand side of equation (24c). The latter process is clearly visible in e.g., Figure 6a in the convergence of wave rays upstream of the ridges, which leads to an increase of perturbed wave energy in that area.

[63] The sensitivity of model results to variations in the parameters is largely determined by the wave-bed form feedback mechanism. The increase in growth rate and migration speed for higher offshore waves is due to the increase in amplitude of the basic state wave orbital velocity and the increase in phase shift between h' and u'_w. However, also bedslope effects increase strongly, which causes the preferred mode to have a larger wavelength (as the downslope movement of sediment is most effective for the small length scales). An increase in wave period leads to similar behavior for the growth rates and migration rates, however the effect is smaller as the magnitude of the basic state orbital velocity and increase in phase shift between h' and

u'_w are limited. Thus changes in the longshore spacing are minor. The large increase in growth rate for an increase in angle of wave incidence at the outer shelf is a consequence of the large increase in phase shift between h' and u'_w. Note that in case of near-normal wave incidence almost no wave refraction is taking place, and thus the wave-bed form feedback mechanism is relatively inefficient compared to the *Trowbridge* [1995] and *Calvete et al.* [2001a] mechanisms.

5.2. Comparison With Observations

[64] The model results have been compared with data of sfcr from different inner shelves. Particular attention has been paid to the alongshore spacing between successive crests, the angle between crestlines and coastline, the cross-shelf extent of the ridges, their growth time and their migration speed.

[65] For the default parameter setting in section 4 (representative for Long Island inner shelf) the most preferred mode is characterized by an alongshore spacing $\lambda \sim 3.1$ km. This is slightly smaller than the observed spacing at this shelf [*Niedoroda and Swift*, 1981; *Schwab et al.*, 2000]. Generally, observed spacings of sfcr range from 2–6 km. Note that Figure 9a indicates that the spacing predicted by the model increases when larger values of the wave height at the outer shelf are taken. In case that $H_{rms,s} = 3$ m the model predicts $\lambda \sim 4.9$ km.

[66] The angle between the coastline and the crest axis obtained with the model in case of the default parameter setting is $\varphi \sim 30°$. Positive values of φ indicate that the ridges are upstream oriented, i.e. their offshore ends are shifted upstream with respect to their attachments at the shoreface. The value of this angle for the ridges that occur at Long Island inner shelf is $\varphi \sim 30–40°$ [*Schwab et al.*, 2000]. Thus, the model predicts the correct orientation of the crests. For experiments with different wave period, offshore wave height or offshore angle of wave incidence

we obtain $\varphi = 30° \pm 5°$. *Duane et al.* [1972] analyzed data of sfcr at different shelves and concluded that most ridges have angles φ between $10°$ and $50°$. Almost all the ridges have positive angles, so they are upstream oriented. This is also predicted by the model.

[67] A noticeable difference between the ridges obtained with the present model and those found with earlier models [*Trowbridge*, 1995; *Calvete et al.*, 2001a] is that they are more trapped to the coast. In the default case the offshore extent of the ridges is 1 km, i.e., about 20% of the width of the inner shelf, whereas the previous models yield ridges that fully cover the shelf. The observed sfcr at Long Island shelf extend about 2.5 km over the shelf, i.e., a coverage of about 50%. Inspection of patterns of sfcr at other shelves, as presented in *Swift et al.* [1978] and *van Meene and van Rijn* [2000] reveals that most ridges occupy about half of the width of the inner shelf. Such values of the cross-shore extent of the ridges are predicted with our model in case that $H_{rms,s}$ is about 3.5 m. We stress that previous models always predict ridges that cover the entire shelf.

[68] Finally, we consider the growth timescale T_g and migration speed V_m of the ridges. The present model yields $T_g \sim 195$ yr and $V_m \sim 33$ m yr^{-1} (downstream migration) for the default case. There are no direct field data of T_g, but considering the lifetime of the ridges (several thousands of years) the model result is satisfactory. With regard to the migration speed, observed values range from $1-50$ m yr^{-1}, depending on the measuring period [*Duane et al.*, 1972; *van de Meene and van Rijn*, 2000]. All ridges migrate in the downstream direction, as is also predicted by the model. In all observational studies it is stressed that storms are highly episodic events and that during a single, severe storm ridges can migrate over longer distances than in an entire year without such a storm. Also, note that the modeled values are subject to high uncertainties. They scale linearly with the time fraction during which storms prevail (here 5% is assumed), the reference concentration near the bed (controlled by parameter $\hat{c}_a$) and the thickness of the suspended load layer (parameter δ). In our model the formulation of $\hat{c}_a$ is that proposed by *van Rijn* [1993], which is inversely proportional to the reference height z_a above the bed where the reference concentration is defined. In the experiments the value of z_a is based on the assumption that there are no dunes and sandwaves present on the bed. However, in reality such relatively small-scale bed forms (compared to the sfcr) are definitely observed. As a consequence, the value of z_a becomes larger and that of $\hat{c}_a$ becomes smaller. A factor of order $5-10$ seems quite plausible.

5.3. Model Simplifications

[69] The observed patterns of sfcr are actually rather complex and the model only describes the gross characteristics. The model used in this study is largely simplified with respect to reality, there might be other processes that affect the growth of ridges in nature. First, in the model radiation stresses exerted by the waves and wave-induced Stokes drift are ignored. Second, the linear stability analysis employed yields no information about the finite amplitude of the ridges. By using a depth-averaged model, the role of the vertical structure of the currents is neglected. However, field data [e.g., *Niedoroda et al.*, 1984] have revealed the presence of vertical circulation cells perpendicular to the coast. This suggests that taking into account 3D processes in the current model is important. Another simplification is the use of one single grain size in the experiments, whereas data clearly show variations in grain size over the ridges. In the present study we consider the microtidal American shelf, for which it is justifiable to consider only storm-driven currents and neglect the relatively weak tidal flows. However, near e.g., the Dutch and German coasts strong tidal currents occur and bottom stresses are sufficiently strong to erode and transport sediment even during fair weather conditions. *Calvete et al.* [2001b] demonstrated that dependent on the actual tidal conditions, intensity of the storm-driven flow and fraction of time during which storms prevail a variety of large-scale bed forms, including tidal sand banks and sfcr, are formed. According to *Walgreen et al.* [2002] overtides can have a large effect on migration speeds of the ridges, but not on their growth rates. It would be interesting to investigate the effect of tidal flow in the context of the present model.

6. Conclusions

[70] In this paper a new model has been discussed that describes the initial formation of sfcr on microtidal inner shelves due to interaction between waves, a storm-driven current along the coast and the sandy bottom. The most distinct differences between the present model and those of *Trowbridge* [1995] and *Calvete et al.* [2001a] is that here the behavior of waves is described by equations which are derived from physical principles, rather than by parameterizations, and that interactions between waves and bed forms are accounted for. Moreover, erosion of sediment now only occurs if the near-bed wave orbital velocity amplitude exceeds a critical value.

[71] For a model setting that resembles the situation at Long Island inner shelf it has been found that the fastest growing modes resemble sfcr of which the offshore ends are shifted upstream with respect to their attachments to the shoreface. Typical alongshore distances between successive crests are several kilometers and the ridges migrate several tens of meters per year. Compared to results obtained with previous models the ridges are more trapped to the coast, only for large wave heights at the outer shelf (>3.5 m) the bed forms extend over the entire shelf. Including a critical velocity for erosion has a tempering effect on the growth.

[72] A physical analysis has revealed that in this model the ridges grow due to three different mechanisms. The first is the one described by *Trowbridge* [1995] which involves the offshore deflection of the current over the ridges over a transversely sloping bottom. The second is described by *Calvete et al.* [2001a] and involves the joint action of cross-shore gradients in the depth-averaged sediment concentration of the reference state (i.e., the state in which bed forms are absent) and the offshore deflection of currents over the ridges. The third is new and is referred to as the wave-bed form feedback mechanism. It significantly contributes to further growth of upstream oriented ridges because the latter cause wave rays to converge (diverge) on the upstream (downstream) sides of the crests. Consequently, focusing (defocusing) of wave energy in these areas occurs, which subsequently results in enhanced (reduced) stirring of sediment by waves, hence also of sediment load, which is

subsequently transported as suspended load by the storm-driven flow. This mechanism is even active in the absence of a transversely sloping bottom and it is more effective than the first two mechanisms. The consequence is that both growth and migration of the ridges are now controlled by suspended load transport of sediment; bed load transport only plays a minor role. Furthermore, the formation of sfcr does not require the presence of a transversely sloping bottom, albeit that model results are in better agreement with field data in case the modeled shelf geometry has such a slope. We conclude that comparison of model results with field data at different shelves is satisfactory, given the large uncertainties in the magnitude of the suspended load sediment transport and in the time fraction during which storms prevail and ridges evolve.

References

Amos, C. L., M. Z. Li, and K.-S. Choung (1996), Storm-generated, hummocky stratification on the outer-Scotian Shelf, *Geo Mar. Lett.*, 16, 85–94.
Anthony, D., and J. O. Leth (2002), Large-scale bed forms, sediment distribution and sand mobility in the eastern North Sea off the Danish west coast, *Mar. Geol.*, 182, 247–263.
Antia, E. E. (1996), Shoreface-connected ridges in German and US Mid-Atlantic bights: similarities and contrasts, *J. Coastal Res.*, 12, 141–146.
Bailard, J. A. (1981), An energetics total load sediment transport model for a plane sloping beach, *J. Geophys. Res.*, 86(C11), 10,938–10,954.
Boyd, J. P. (2001), *Chebyshev and Fourier Spectral Methods*, Dover, New York.
Calvete, D., A. Falqués, H. E. de Swart, and M. Walgreen (2001a), Modelling the formation of shoreface-connected sand ridges on storm-dominated inner shelves, *J. Fluid Mech.*, 441, 169–193.
Calvete, D., M. Walgreen, H. E. de Swart, and A. Falqués (2001b), A model for sand ridges on the shelf: Effect of tidal and steady currents, *J. Geophys. Res.*, 106(C5), 9311–9325.
Calvete, D., N. Dodd, A. Falqués, and S. M. van Leeuwen (2005), Morphological development of rip channel systems: Normal and near-normal wave incidence, *J. Geophys. Res.*, 110, C10006, doi:10.1029/2004JC002803.
Draper, L. (1991), Wave climate atlas of the British isles, *Tech. Rep. Offshore Technol. Rep. OTH 89 303*, Dep. of Energy, HMSO, London.
Duane, D. B., M. E. Field, E. P. Miesberger, D. J. P. Swift, and S. J. Williams (1972), Linear shoals on the Atlantic continental shelf, Florida to Long Island, in *Shelf Sediment Transport: Process and Pattern*, edited by D. J. P. Swift, D. B. Duane, and O. H. Pilkey, pp. 447–498, Dowden, Hutchinson and Ross, Stroudsburg, Pa.
Dyer, K. R., and D. A. Huntley (1999), The origin, classification and modelling of sand banks and ridges, *Cont. Shelf Res.*, 19, 1285–1330.
Edwards, J. H., S. E. Harrison, S. D. Locker, A. C. Hine, and D. C. Twichell (2003), Stratigraphic framework of sediment-starved sand ridges on a mixed siliciclastic/carbonate inner shelf; west-central Florida, *Mar. Geol.*, 200, 195–217.
Falqués, A., D. Calvete, and H. E. de Swart (1998), Morphodynamics of shoreface-connected ridges, in *Coastal Engineering 1998*, edited by B. L. Edge, pp. 2851–2864, Am. Soc. of Civ. Eng., Reston, Va.
Figueiredo, A. G., J. E. Sanders, and D. J. P. Swift (1982), Storm-graded layers on inner continental shelves: Examples from southern Brazil and the Atlantic coast of the central United States, *Sediment. Geol.*, 31, 171–190.
Green, M., C. E. Vincent, I. N. McCave, R. R. Dickson, J. M. Rees, and N. Pearson (1995), Storm sediment transport: observations from the British North Sea shelf, *Cont. Shelf Res.*, 15(8), 889–912.
Harrison, S. E., S. D. Locker, A. C. Hine, J. H. Edwards, D. F. Naar, and D. C. Twichell (2003), Sediment-starved sand ridges on a mixed carbonate/siliciclastic inner shelf off west-central Florida, *Mar.*, 200.
Hoogendoorn, E. L., and R. W. Dalrymple (1986), Morphology, lateral migration and internal structures of shoreface-connected ridges, Sable Island Bank, Nova Scotia, Canada, *Geology*, 14, 400–403.
Komen, G. J., L. Cavaleri, M. Donelan, K. Hasselmann, S. Hasselmann, and P. A. E. M. Janssen (1994), *Dynamics and Modelling of Ocean Waves*, Cambridge Univ. Press, New York.
Lentz, S., R. T. Guza, S. Elgar, F. Feddersen, and T. H. C. Herbers (1999), Momentum balances on the North Carolina Inner Shelf, *J. Geophys. Res.*, 104(C8), 18,205–18,226.
Longuet-Higgins, M. S. (1980), On the statistical distribution of the heights of sea waves, *J. Geophys. Res.*, 75(33), 6778–6801.
McBride, R. A., and T. F. Moslow (1991), Origin, evolution, and distribution of shoreface sand ridges, Atlantic inner shelf, U.S.A., *Mar. Geol.*, 97, 57–85.
McClennen, C. E., and R. L. McMaster (1971), Probable holocene transgressive effects on the geomorphic features of the continental shelf off New Jersey, United States, *Marit. Sediments*, 7, 69–72.
Mei, C. C., M. Stiassnie, and D. K.-P. Yue (2005), *Theory and Applications of Ocean Surface Waves Part 1: Linear Aspects*, World Sci., Singapore.
Niedoroda, A. W., and D. J. P. Swift (1981), Maintenance of the shoreface by wave orbital currents and mean flow: observations from the Long Island coast, *Geophys. Res. Lett.*, 8, 337–340.
Niedoroda, A. W., D. J. P. Swift, T. S. Hopkins, and C. H. Ma (1984), Shoreface morphodynamics on wave-dominated coasts, *Mar. Geol.*, 60, 331–354.
Parker, G., N. W. Lanfredi, and D. J. P. Swift (1982), Seafloor response to flow in a Southern Hemisphere sand-ridge field: Argentina inner shelf, *Sediment. Geol.*, 33, 195–216.
Restrepo, J. M. (2001), Wave-current interactions in shallow waters and shore-connected ridges, *Cont. Shelf Res.*, 21, 1331–1360.
Schwab, W. C., E. R. Thieler, J. R. Allen, D. S. Foster, B. A. Swift, and J. F. Denny (2000), Influence of inner-continental shelf geologic framework on the evolution and behavior of the barrier-island system between Fire Island Inlet and Shinnecock Inlet, Long Island, New York, *J. Coastal Res.*, 16(2), 408–422.
Swift, D. J. P., and M. E. Field (1981), Evolution of a classic sand ridge field: Maryland sector, North American inner shelf, *Sedimentology*, 28, 461–482.
Swift, D. J. P., B. Holliday, N. Avignone, and G. Shideler (1972), Anatomy of a shoreface ridge system, False Cape, Virginia, *Mar. Geol.*, 12, 59–84.
Swift, D. J. P., G. Parker, N. W. Lanfredi, G. Perillo, and K. Figge (1978), Shoreface-connected sand ridges on American and European shelves: a comparison, *Estuarine Coastal Mar. Sci.*, 7, 257–273.
Trowbridge, J. H. (1995), A mechanism for the formation and maintenance of the shore oblique sand ridges on storm-dominated shelves, *J. Geophys. Res.*, 100(C8), 16,071–16,086.
Twichell, D., G. Brooks, G. Gelfenbaum, V. Paskevich, and B. Donahue (2003), Sand ridges off Sarasota, Florida: A complex facies boundary on a low-energy inner shelf environment, *Mar. Geol.*, 200, 243–262.
van de Meene, J. W. H., and L. C. van Rijn (2000), The shoreface-connected ridges along the central Dutch coast. part 1: field observations, *Cont. Shelf Res.*, 20(17), 2295–2323.
van Rijn, L. C. (1993), *Principles of Sediment Transport in Rivers, Estuaries and Coastal Seas*, Aqua, Amsterdam.
Walgreen, M., D. Calvete, and H. E. de Swart (2002), Growth of large-scale bed forms due to storm-driven and tidal currents: a model approach, *Cont. Shelf Res.*, 22(18–19), 2777–2793.
Williams, J. J., C. P. Rose, P. D. Thorne, B. A. O'Connor, J. D. Humphery, P. J. Hardcastle, S. P. Moores, J. A. Cooke, and D. J. Wilson (1999), Field observations and predictions of bed shear stresses and vertical suspended sediment concentration profiles in wave-current conditions, *Cont. Shelf Res.*, 19, 507–536.

————————
D. Calvete, Departament de Física Aplicada, Universitat Politécnica de Catalunya, Campus Nord - Modùl B4, 08034 Barcelona, Spain. (calvete@fa.upc.edu)
H. E. de Swart and N. C. Vis-Star, Institute for Marine and Atmospheric Research Utrecht, Utrecht University, Princetonplein 5, 3584 CC Utrecht, Netherlands. (h.e.deswart@phys.uu.nl; n.c.vis-star@phys.uu.nl)